RSC Advances

PAPER

View Article Online
View Journal | View Issue

Cite this: *RSC Adv.*, 2021, **11**, 16661

Cytotoxicity and cell imaging of six types of carbon nanodots prepared through carbonization and hydrothermal processing of natural plant materials

Yu-Yu Chen,[a] Wen-Ping Jiang,[bc] Huan-Luen Chen,[a] Hui-Chi Huang,[de] Guan-Jhong Huang,[d] Hsiu-Mei Chiang,[a] Chang-Cheng Chang,[fg] Cheng-Liang Huang[h] and Tzong-Yuan Juang *[a]

In this study we prepared six types of carbon nanodots (CNDs) from natural plant materials – through carbonization of two species of bamboo (Bamboo-I, Bamboo-II) and one type of wood (Wood), and through hydrothermal processing of the stem and root of the herb *Mahonia oiwakensis* Hayata (MO) and of the agricultural waste of two species of pineapple root (PA, PB). The resulting CNDs were spherical with dimensions on the nanoscale (3–7 nm); furthermore, CND-Bamboo I, CND-Wood, CND-Bamboo II, CND-MO, CND-PA, and CND-PB displayed fluorescence quantum yields of 9.63, 12.34, 0.90, 10.86, 0.35, and 0.71%, respectively. X-ray diffraction revealed that the carbon nanostructures possessed somewhat ordered and disordered lattices, as evidenced by broad signals at values of 2θ between 20 and 30°. CND-Bamboo I, CND-Wood, and CND-Bamboo II were obtained in yields of 2–3%; CND-MO, CND-PA, and CND-PB were obtained in yields of 17.64, 9.36, and 22.47%, respectively. Cytotoxicity assays for mouse macrophage RAW264.7 cells treated with the six types of CNDs and a commercial sample of Ag nanoparticles (NPs) revealed that each of our CNDs provided a cell viability of 90% at 2000 μg mL^{-1}, whereas it was only 20% after treatment with the Ag NPs at 62.5 μg mL^{-1}. The six types of CNDs also displayed low cytotoxicity toward human keratinocyte HacaT cells, human MCF-7 breast cancer cells, and HT-29 colon adenocarcinoma cells when treated at 500 μg mL^{-1}. Moreover, confocal microscopic cell imaging revealed that the fluorescent CND-Bamboo I particles were located on the MCF-7 cell membrane and inside the cells after treatment for 6 and 24 h, respectively. We have thoroughly investigated the photoluminescence properties and carbon nanostructures of these highly dispersed CNDs. Because of the facile green synthesis of these six types of CNDs and their sourcing from abundant natural plants, herbs, and agriculture waste, these materials provide a cost-effective method, with low cytotoxicity and stable fluorescence, for biolabeling and for developing cell nanocarriers.

Received 18th February 2021
Accepted 29th April 2021

DOI: 10.1039/d1ra01318a

rsc.li/rsc-advances

1. Introduction

Carbon nanodots (CNDs), individual graphene nanosheets, carbon nanotubes, nanodiamonds, and non-conventional fluorescent polymer dots are attracting considerable interest as carbon nanomaterials with uses ranging from high-performance electrochemistry to biomaterials.[1–7] In particular, CNDs are attractive for their adjustable photoluminescence (PL) characteristics, multicolor emissions, excellent long-term photostability (non-photobleaching behavior),[8–11] low cost, and facile preparation and functionalization.[12–14] The PL of CNDs having particle sizes of less than 10 nm has been attributed to quantum confinement effects and the nature of their surface functional groups, both of which lead to changes in energy band gaps and, therefore, tunable emission characteristics.[15] The presence of oxygen-rich functional groups on a CND surface can also result in highly dispersed aqueous solutions.[16,17] The preparation of CNDs can be divided into "bottom up" (synthesized from small molecules) and "top down" (cut from larger carbon materials) approaches.[1,18] CNDs have been prepared from various bio-resources, including hair, milk, and garlic.[19–21] Nair, *et al.* also prepared CNDs from snake gourd peel and applied them to the analysis of Fe^{3+} ions.[22] Herein, we prepared our CNDs from various natural plants as precursors, providing

[a]*Department of Cosmeceutics, China Medical University, Taichung, Taiwan. E-mail: tyjuang@mail.cmu.edu.tw*
[b]*Department of Occupational Therapy, Asia University, Taichung, Taiwan*
[c]*Department of Pharmacy, Chia Nan University of Pharmacy and Science, Tainan, Taiwan*
[d]*Department of Chinese Pharmaceutical Sciences and Chinese Medicine Resources, China Medical University, Taichung, Taiwan*
[e]*Master Program for Food and Drug Safety, China Medical University, Taichung, Taiwan*
[f]*Aesthetic Medical Center, China Medical University Hospital, Taichung, Taiwan*
[g]*School of Medicine, China Medical University, Taichung, Taiwan*
[h]*Department of Applied Chemistry, National Chiayi University, Chiayi, Taiwan*

an eco-friendly synthesis and a means of recycling agricultural waste. The most attractive features for a CND are ease of synthesis, a variety of fluorescence properties, low cytotoxicity, and high biocompatibility.[23,24]

CNDs have been used in biomedicine as antibacterial and anticancer agents and for wound healing and bioimaging.[25–28] Relative to metal nanoparticles (NPs), CNDs constructed from carbon materials are relatively low in toxicity toward organisms and the environment.[23] The surfaces of CNDs can be modified and conjugated with various active compounds (*e.g.*, protein drugs) for application in biosensors and drug delivery systems.[27,29,30] Hydrophilic CND-drug conjugates are also useful as drug carriers because their ability to experience multi-hydrogen-bonding interactions means that they disperse well in aqueous solutions.[31,32] For example, Wang *et al.* prepared a CND from commercial beer and conjugated it with doxorubicin hydrochloride for application in an anticancer treatment protocol.[33]

Because of their antibacterial properties, CNDs have been applied in biomedical materials for effective wound dressing and disinfection. For example, Bankoti *et al.* prepared onion-derived CNDs for accelerated skin wound healing (within two weeks) in a rat model.[34] Omidi *et al.* used a CND/chitosan hydrogel for wound dressing; the CNDs displayed antibacterial properties in a disc diffusion assay, with the resulting CND/chitosan hydrogel exhibiting complete healing in a rat skin wound model after 18 days.[27] Huang *et al.* synthesized spermidine-capped fluorescent carbon quantum dots (Spd-CQDs) displaying antibacterial properties; the minimum inhibitory concentration (MIC) of the Spd-CQDs reached as low as 0.9 μg mL^{-1} (*cf.* 12 μg mL^{-1} for the Ag NPs) for the treatment of bacterial methicillin-resistant *S. aureus*.[35] These CNDs were further developed as biomedicinal materials for skin wound dressing and antibacterial eye drops.[27,36] Although Ag NPs possess remarkable antibacterial effects, they display *in vitro* cytotoxicity with half maximal inhibitory concentrations (IC_{50}) toward Ehrlich's ascites carcinoma (EAC), Jurkat, and MCF-7 cell lines of 5.6, 11.99, and 13.33 μg mL^{-1}, respectively.[23] Moreover, Lee *et al.* found that Ag NPs induced the excessive formation of reactive oxygen species (ROS) and, therefore, displayed cytotoxicity toward NIH 3T3 cells.[37,38]

In this study, we prepared six types of CNDs through a carbonization process [with two species of bamboo (Bamboo-I, Bamboo-II) and one of wood (Wood)] and through a hydrothermal process [with the stem and root of the herb *Mahonia oiwakensis* Hayata (MO) and with the agricultural waste of two species of pineapple root (PA, PB)]. We characterized these CNDs in terms of their carbon nanostructures and their cytotoxicity [through 3-(4,5-dimethylthiazol-2-yl)-2,5-diphenyltetrazolium bromide (MTT) assays] toward four cell lines. The MO herb stem and root were collected from Taiwan Ali mountain.[39,40] Bamboo I was calcined under unified conditions in a stainless-steel autoclave at 1100 °C for 96 h.[6] Our six types of CNDs displayed fluorescence, and their lattices existed between ordered and disordered carbon nanostructures; they possessed a variety of oxygen-rich functional groups depending on their natural plant sources. CND-Bamboo I, CND-Wood, and CND-Bamboo II had oxygen atom contents of greater than 30 wt%. CND-MO, CND-PA, and CND-PB were nitrogen-doped CNDs; X-ray photoelectron spectroscopy (XPS) revealed nitrogen atom contents of greater than 5 wt%. The cell viability MTT assays revealed low cytotoxicity for our six CNDs toward RAW 264.7 cells at a loading of 2000 μg mL^{-1} and toward HacaT, MCF-7, and HT-29 cells at 500 μg mL^{-1}, making them potentially useful as biomedicinal nanocarriers and for bioimaging.

2. Materials and methods

2.1 Preparation of six types of CND

CND-Bamboo I and CND-Bamboo II, CND-Wood, CND-MO, and CND-PA and CND-PB were prepared from bamboo, wood, *Mahonia oiwakensis* Hayata, and pineapple precursors, respectively. Bamboo I was calcined in a stainless-steel autoclave at 1100 °C for 96 h, forming a black material. The carbonized Bamboo II and carbonized Wood were purchased from Shun-Yi Chemicals (Taiwan). The *Mahonia oiwakensis* Hayata stem and root and the pineapple root were dried through exposure to sunlight. The carbonized bamboo, carbonized wood, and dry natural MO herb and pineapple were ground into powders. For CND-Bamboo I, CND-Wood, and CND-Bamboo II, the powder (5 g) was placed in a beaker and treated with deionized water (100 mL). Each mixture was stirred thoroughly and adjusted to pH 12.00 with 1 M NaOH. The CNDs of the carbonized bamboo and carbonized wood were extracted into the aqueous phase at 80 °C for 2 h. For CND-MO, CND-PA, and CND-PB, the CNDs from the MO natural herb and pineapple source were treated hydrothermally at 120 °C under 1.2 kg cm^{-2} for 3 h; each resulting mixture was centrifuged (6000 rpm, 30 min) and then the supernatant was filtered through a 0.22 μm membrane to remove any solid residues. The filtered aqueous CND solutions were then subjected to dialysis through a membrane having a molecular weight cut-off of 3500 g mol^{-1} to remove small-molecule impurities, providing CND-MO, CND-PA, and CND-PB; each CND solution was concentrated and dried in a vacuum oven to obtain the yield of the CND powder.

2.2 Characterization of CNDs

Fluorescence spectra were recorded using a LS-50B luminescence spectrometer (PerkinElmer). UV-Vis spectra were recorded using an UV-1700 spectrophotometer (Shimadzu). High-resolution transmission electron microscopy (HRTEM) was performed using a JEOL-2010 microscope (Japan) operated at an acceleration voltage of 200 kV. X-ray diffraction (XRD) was performed using a Bruker D8 Discover with Cu Kα radiation, at 40 kV and 40 mA. Fourier transform infrared (FTIR) spectra were recorded using an IRAffinity-1S spectrometer (Shimadzu). XPS was performed using a PHI 5000 VersaProbe (ULVAC-PHI); the X-ray source was Al Kα excitation. Bioimaging was preformed using a Leica TCS SP8 X confocal spectral microscope imaging system and a white-light laser.

Quantum yields (QYs) were estimated from the absorption and fluorescence spectra of the CNDs, according to the relative fluorescence QY equation:[41,42]

$$\Phi_{CND} = \Phi_{st}(I_{CND}/I_{st})(\eta/\eta_{st})^2$$

where Φ_{CND} is the QY of the CND, Φ_{st} is the QY of the standard, I is the slope of the plot of the integrated fluorescence intensity with respect to absorbance, and η is the refractive index of the solvent. The standard was quinine sulfate in 0.1 M H_2SO_4; its QY was 54%.

d-Spacings were calculated according to Bragg's law:

$$n\lambda = 2d\sin(\theta)$$

where n is a positive integer, λ is the incident wavelength of the X-rays ($\lambda = 1.5418$ Å), and θ is the diffraction angle.

2.3 Cytotoxicity of CNDs

The cytotoxicities of the six CNDs toward RAW264.7, HacaT, MCF-7, and HT-29 cells were evaluated using MTT assays. HacaT, MCF-7, and HT-29 cells were seeded at 5000 cells per well in 96-well plates and cultured in fresh Dulbecco's modified Eagle's medium (DMEM) containing 10% fetal bovine sera (FBS) and 1% antibiotic at 37 °C with 5.0% CO_2. Each CND stock solution was prepared at a concentration of 25 mg mL^{-1} in phosphate-buffered saline (PBS) and filtered through a 0.22 μm membrane. Various concentrations of the CND solutions were prepared in PBS and added to DMEM. The HacaT and MCF-7 cells were treated with various concentrations of the CND solutions for 48 h. The HT-29 cells were also treated with the CND solutions for 48 h. The MTT stock solution (5 mg mL^{-1}) was added at 20 μL per well and reacted for 2–4 h; the supernatant was discarded and DMSO (200 μL) was added. Detection was performed using a SpectraMax® M2e instrument at OD_{570}.

Commercial Ag NPs (NanoAg) were purchased as a 5000 ppm stock solution from Ching-Tai Resins chemical company. The *in vitro* cell viability activities of the CNDs and NanoAg were determined using MTT assays. RAW264.7 cells (5×10^4 cells per well) were seeded in 96-well plates and incubated for 24 h. The cells were treated with the CNDs and NanoAg at various

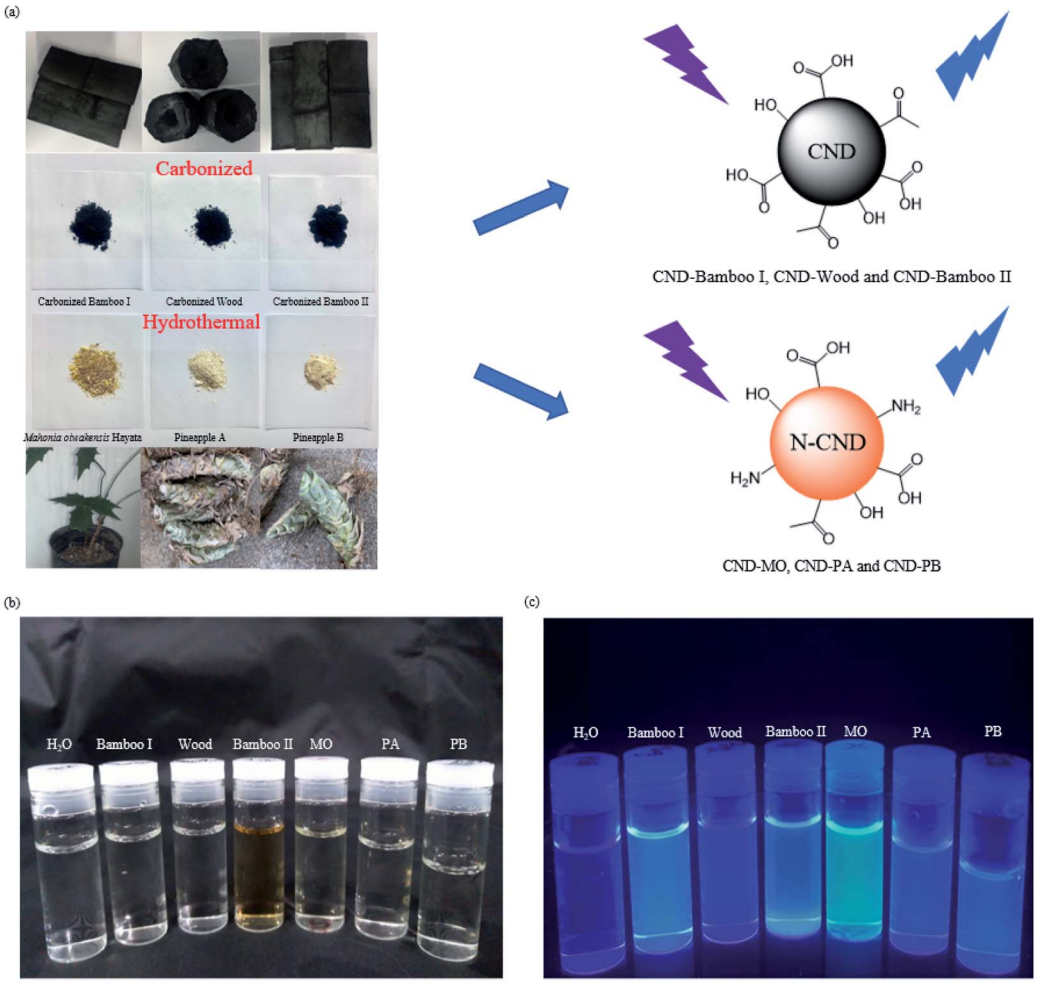

Fig. 1 (a) Schematic representation of the preparation of six types of CNDs from different raw natural plants. (b) and (c) Photographs of solutions of CNDs exposed to (b) daylight and (c) UV light; from left to right: CND-Bamboo I, CND-Wood, CND-Bamboo II, CND-MO, CND-PA, and CND-PB in deionized water.

concentrations (0, 15.6, 62.5, 250, 500, 1000, and 2000 μg mL^{-1}) for 24 h. The medium was replaced with a medium containing 0.5 mg mL^{-1} of MTT solution and then the mixture was incubated at 37 °C for 4 h. After the end of the MTT reaction, the supernatant was discarded and DMSO (200 μL) was added. Detection was performed using a SpectraMax® M2e instrument at OD_{570}. The cell viability was calculated and compared with that of the control group.

2.4 *In vitro* nitric oxide (NO) production of the CNDs and NanoAg

The mouse macrophage RAW264.7 cell line was cultured in DMEM containing 10% FBS, penicillin and streptomycin (100 U mL^{-1}), and 4 mM L-glutamine (100 U mL^{-1}). The cells were cultured in a humidified incubator under 5% CO_2 at 37 °C.

RAW264.7 cells (5×10^4 cells per well) were seeded in 96-well plates and incubated for 24 h. The cells were treated with the CNDs and NanoAg at various concentrations (0, 15.6, 62.5, 250, 500, 1000, and 2000 μg mL^{-1}), and with a positive control of lipopolysaccharides (LPS, 100 ng mL^{-1}), for 24 h. For the NO assay, the supernatant was collected from the cell culture and mixed with an equal volume of Griess reagent (1% sulphanilamide, 0.1% naphthylethylenediamine dihydrochloride, 5% phosphoric acid) and the absorbance measured at OD_{570} using the SpectraMax® M2e instrument.

2.5 Cell imaging

HacaT and MCF-7 cells were seeded (1×10^5 cells per well) in a 6-well plate and cultured in fresh DMEM containing 10% FBS and 1% antibiotic at 37 °C under 5.0% CO_2 for 24 h. The concentrations of the CND-Bamboo I and CND-MO stock solutions were each 25 mg mL^{-1} in PBS; the solutions were filtered through a 0.22 μm membrane. The HacaT and MCF-7 cells were treated with CND-Bamboo I and CND-MO for 6 h; the concentrations of CND-Bamboo I and CND-MO were each 500 μg mL^{-1} in the medium. HacaT and MCF-7 cells were seeded (5×10^5 cells per well) in a 6-well plate in fresh DMEM at 37 °C under 5.0% CO_2 for 24 h. The HacaT and MCF-7 cells were treated with CND-Bamboo I and CND-MO for 24 h; the concentrations of CND-Bamboo I and CND-MO were each 500 μg mL^{-1} in the medium.

3. Results and discussion

For the preparation of our CNDs, we used natural plants as renewable carbon sources and subjected them to carbonization or hydrothermal processes to construct the carbon nanostructures. Our CND-Bamboo I was obtained through calcination of bamboo at 1100 °C and subsequent extraction into water. We purchased CND-Wood and CND-Bamboo II from Shun-Yi Chemicals (Taiwan); they had also been subjected to calcination, but we could be more certain of the conditions for the preparation of CND-Bamboo I.[6] The optimized pH for the preparation of the CNDs from the calcined bamboo and wood was adjusted with 1 M NaOH from the original pH 10 to 12. The CNDs from CND-MO, CND-PA, and CND-PB were obtained under hydrothermal conditions at 120 °C in an autoclave for 3 h. When performing the hydrothermal method at high temperature and pressure for various periods of time, we found that the QYs were greatest after 3 h. The pH of the solutions of these carbonized precursors was adjusted to pH 12 to increase the yields of the CNDs (*i.e.*, by allowing effective separation from the precursor by deprotonating the oxygen-containing functional groups).[43] Performing the hydrothermal process at pH 12 not only allowed effective separation of the product but also allowed NaOH to function as a catalyst.[44] The CND purification

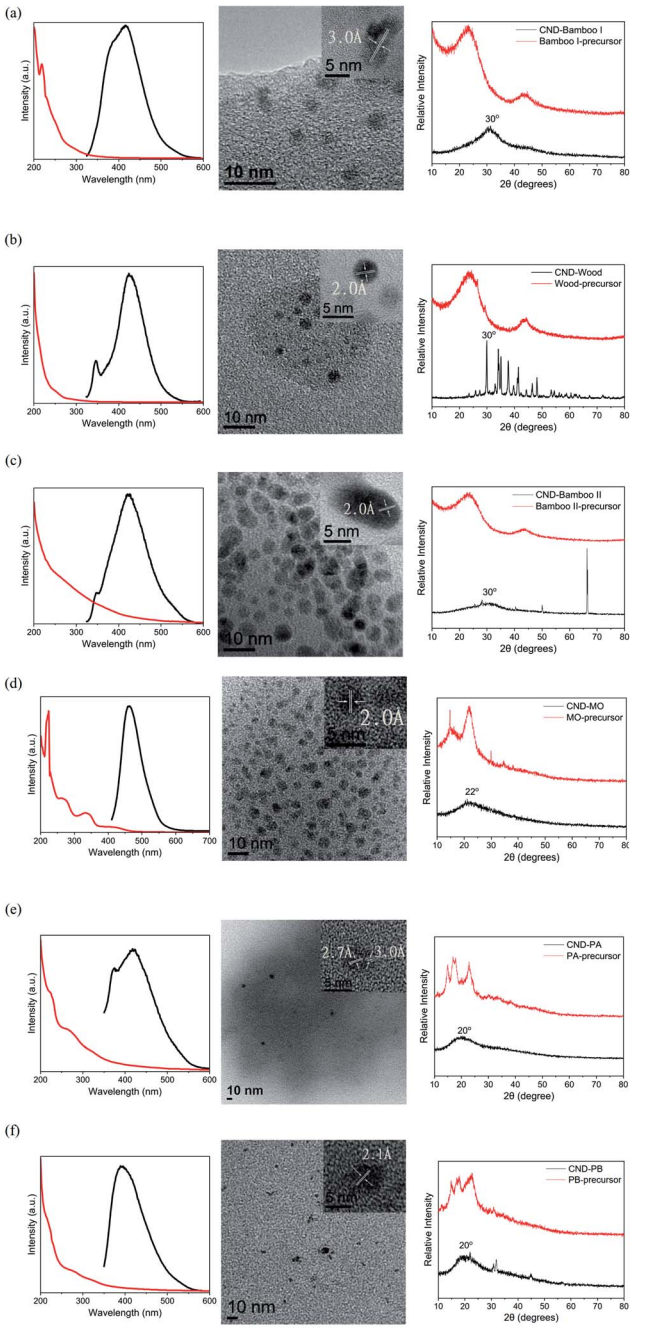

Fig. 2 PL (black line) and UV-Vis absorption (red line) spectra, HRTEM images, and XRD patterns of (a) CND-Bamboo I, (b) CND-Wood, (c) CND-Bamboo II, (d) CND-MO, (e) CND-PA, and (f) CND-PB.

process consisted of filtration and dialysis. Filtration through a membrane removed any insoluble particles that formed in the reaction, while dialysis removed small-molecule impurities. Finally, the dialyzed solution of CNDs was dried in a vacuum oven to provide a CND powder. The yields of CND-Bamboo I, CND-Wood, CND-Bamboo II, CND-MO, CND-PA, and CND-PB were 2.27, 2.01, 2.91, 17.64, 9.36, and 22.47%, respectively. Our CNDs displayed fluorescence when exciting their aqueous solutions at 365 nm (Fig. 1).

We recorded PL spectra to measure the fluorescence of the CNDs derived from the carbonized bamboo, carbonized wood, natural herb, and pineapple. After exciting our CNDs at various wavelengths, we selected an excitation wavelength that provided an emission of relatively high intensity. The spectra of CND-Bamboo I, CND-Wood, and CND-Bamboo II were recorded with excitation at a wavelength of 310 nm (Fig. 2a–c); those of the CNDs of MO and the pineapples were obtained with excitation at 390 and 330 nm, respectively (Fig. 2d–f). The solutions of CND-Bamboo I, CND-Wood, and CND-Bamboo II provided emission wavelengths of 420, 425, and 425 nm, respectively; the emission wavelengths of CND-MO, CND-PA, and CND-PB were 465, 420, and 390 nm, respectively (Fig. 2d–f). The UV-Vis absorption spectra of CND-Bamboo I, CND-Wood, and CND-Bamboo II featured a signal at a wavelength from 200 to 300 nm for the π–π* transitions of their C=C bonds (Fig. 2a–c).[45,46] A long wavelength tail extending to the visible region, ascribed to the n–π* transitions of C=O bonds, appeared in the spectrum of CND-Bamboo II.[9,47] The spectra of CND-MO, CND-PA, and CND-PB featured signals for the π–π* transitions of their C=C bonds at 200–300 nm; the n–π* transitions of their C=O or amine groups appeared at 300–400 nm (Fig. 2d–f).[48–50] The QYs of the CNDs were calculated from their UV-Vis absorption and fluorescence spectra. The UV-Vis absorptions were measured at 310 nm for CND-Bamboo I, CND-Wood, and CND-Bamboo II, 390 nm for CND-MO, and 330 nm for CND-PA and CND-PB; these were the excitation wavelengths that provided relatively high emission intensities. From the UV-Vis absorption and fluorescence spectra, we calculated the QYs of CND-Bamboo I, CND-Wood, CND-Bamboo II, CND-MO, CND-PA, and CND-PB to be 9.63, 12.34, 0.90, 10.86, 0.35, and 0.71%, respectively (Table 1).

Fig. 2a–f also display the XRD patterns, HRTEM-analyzed lattices, and particle sizes of the six types of CNDs. The signals in the XRD patterns of the precursors of CND-Bamboo I, CND-Wood, and CND-Bamboo II were divided mainly into two peaks, located at values of 2θ of 23 and 43°. XRD revealed that the characteristic peaks of CND-Bamboo I, CND-Wood, and CND-Bamboo II, obtained after extracting the carbonized precursors, appeared at 30° (Fig. 2a–c). Placing these values of 2θ for CND-Bamboo I, CND-Wood, and CND-Bamboo II into the Bragg equation gave *d*-spacings of 3.0 Å. The XRD patterns of CND-Bamboo I, CND-Wood, and CND-Bamboo II also featured broad peaks that corresponded to the (002) planes of graphite; the typical (002) plane appears near 26.5°, suggesting that CND-Bamboo I, CND-Wood, and CND-Bamboo II were CNDs of high oxygen content.[51,52] The carbonized wood was, however, incompletely carbonized, because its XRD peak was disordered and non-broad.[53] The carbonized Bamboo I was calcined in a stainless-steel autoclave at 1100 °C for 96 h; CND-Bamboo I was present in the coordinated CNDs, characterized by a broad peak and an ordered lattice in the XRD and HRTEM analyses, respectively.[54,55] The carbonized wood and carbonized Bamboo II were purchased as commercial materials; their calcination conditions were less well defined, and these CNDs provided more disordered spectra. The collocation of the HRTEM images revealed different planes for CND-Bamboo I, corresponding to the (002) plane of graphite, and for CND-Wood and CND-Bamboo II, corresponding to the (100) plane of graphitic carbon; the average lattice spacings were 3.0, 2.0, and 2.0 Å, respectively (Fig. 2a–c).[56,57] The particle sizes of CND-Bamboo I, CND-Wood, and CND-Bamboo II were approximately 3–4, 3–4, and 4–5 nm, respectively.

Fig. 2d–f present the XRD patterns of CND-MO, CND-PA, and CND-PB, respectively; they revealed signals at values of 2θ of 22, 20, and 20°, respectively, giving *d*-spacings of 4.0, 4.4, and 4.4 Å, respectively, corresponding to the (002) plane of graphite.[58–60]

Table 1 Properties of CNDs prepared from various source materials

			PL	QY[b]		Particle size[c]	Atomic composition[d] (%)		
Name	Source	Yield (%)	Ex[a] (nm)	Em (nm)	(%)	(nm)	C	O	N
Carbonized, water-extracted at 80 °C, 2 h, pH 12									
CND-Bamboo I	Bamboo	2.27	310	420	9.63	4.0 ± 0.3	52.8	47.2	<0.1
CND-Wood	Wood	2.01	310	425	12.34	3.7 ± 0.4	52.4	47.6	<0.1
CND-Bamboo II	Bamboo	2.91	310	425	0.90	4.4 ± 0.7	66.0	34.0	<0.1
Hydrothermal, 120 °C, 3 h, pH 12									
CND-MO	*Mahonia oiwakensis* Hayata	17.64	390	465	10.86	3.5 ± 0.9	66.9	28.0	5.1
CND-PA	Pineapple	9.36	330	420	0.35	2.7 ± 0.3	67.2	25.9	6.9
CND-PB	Pineapple	22.47	330	390	0.71	3.3 ± 0.8	63.7	24.0	12.3

[a] Determined through fluorescence spectroscopy, using excitation wavelengths that provided relatively high intensity emissions. [b] Calculated from UV-Vis absorption and integrated fluorescence spectra, according to the equation of relative fluorescence QY. [c] Determined through dynamic light scattering of average particle size. [d] Determined through XPS analysis.

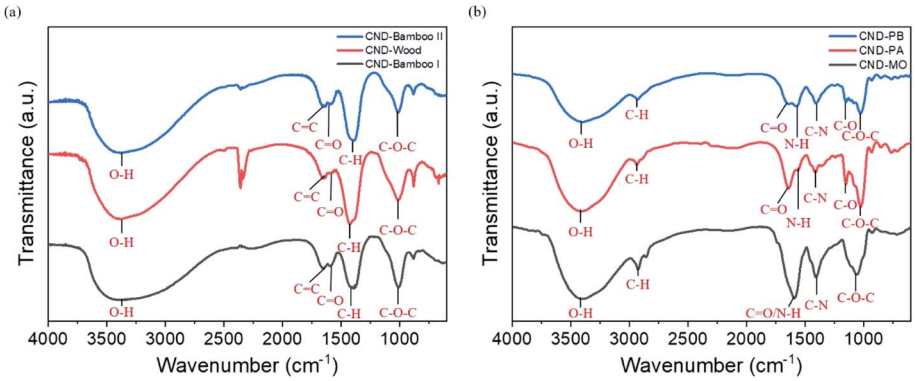

Fig. 3 FTIR spectra of (a) CND-Bamboo I, CND-Wood, and CND-Bamboo II and (b) CND-MO, CND-PA, and CND-PB.

The patterns of the precursors of CND-MO, CND-PA, and CND-PB suggested cellulose structures with values of 2θ between 10 and 30°.[61,62] The HRTEM images of CND-MO and CND-PB revealed, however, lattice spacings of 2.0 and 2.1 Å, respectively, corresponding to the (100) plane of graphene.[63] The HRTEM image of CND-PA revealed spacings of 2.7 and 3.0 Å, corresponding to the (020) and (002) planes of graphitic carbon.[56,64] The particle sizes of CND-MO, CND-PA, and CND-PB were approximately 4–5, 6–7, and 3–4 nm, respectively.

The FTIR spectra of CND-Bamboo I, CND-Wood, and CND-Bamboo II featured signals for O–H stretching, C=C stretching, C=O stretching, C–H bending, and C–O–C stretching at

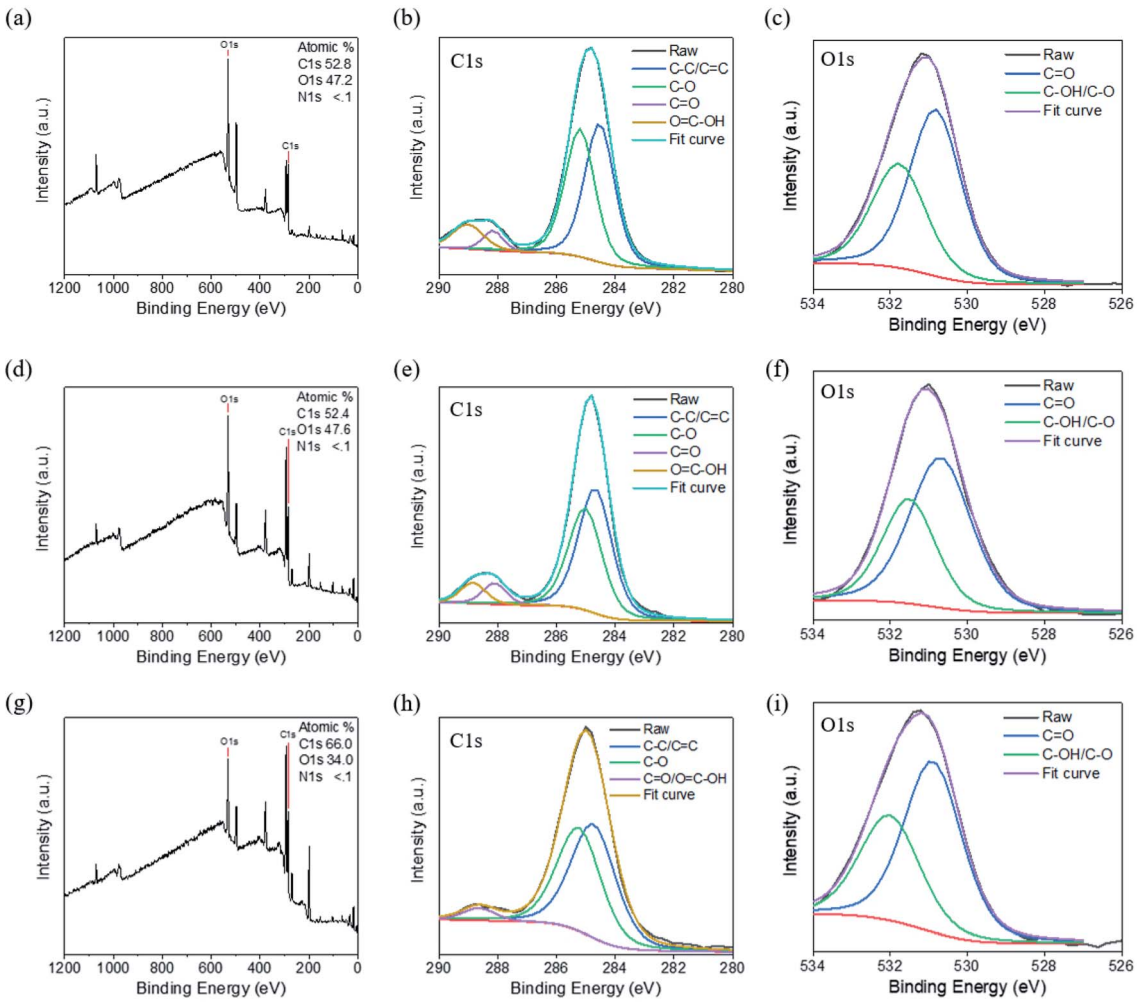

Fig. 4 XPS spectra of (a)–(c) CND-Bamboo I, (d)–(f) CND-Wood, and (g)–(i) CND-Bamboo II: (a), (d) and (g) survey spectra; (b), (e) and (h) C 1s spectra; (c), (f) and (i) O 1s spectra.

3300–3400, 1633–1657, 1573–1593, 1390–1425, and 1013 cm^{-1}, respectively (Fig. 3a).[65–67] The FTIR spectra of CND-PA and CND-PB displayed signals for O–H stretching, C–H stretching, C=O stretching, N–H deformation, C–N stretching, C–O stretching, and C–O–C stretching at 3414–3419, 2910–2935, 1647, 1558–1570, 1408–1417, 1153, and 1024 cm^{-1}, respectively (Fig. 3b).[67–70] The FTIR spectrum of CND-MO featured signals for O–H stretching, C–H stretching, C=O stretching/N–H deformation, C–N stretching, and C–O–C stretching at 3385, 2854–2926, 1595, 1409, and 1055 cm^{-1}, respectively (Fig. 3b).[65,67,68,70,71] Moreover, in the FTIR spectra of our CND samples, especially for CND-Wood, we observed signals for CO_2 at 2300 cm^{-1}, presumably due to their porosity leading to the absorption of CO_2 from the air. Thus, after the carbonization processes, the FTIR spectra of CND-Bamboo I, CND-Wood, and CND-Bamboo II revealed that they had similar oxygen atom functionalities. In contrast, the FTIR spectra of CND-MO, CND-PA, and CND-PB revealed both nitrogen and oxygen atoms functionalities, because their precursor plants contained both nitrogen and oxygen atoms.

We performed further XPS analyses of the CNDs to characterize their chemical structures. Fig. 4a reveals that CND-Bamboo I contained carbon (52.8%) and oxygen (47.2%) atoms. Fig. 4b displays the C 1s binding energies, revealing signals for C–C/C=C (284.5 eV), C–O (285.2 eV), C=O (288.2 eV), and O=C–OH (289.0 eV) species. Fig. 4c displays the O 1s binding energies, revealing C=O (530.8 eV) and C–OH/C–O (531.8 eV) functionalities. The elements present in CND-Wood were carbon (52.4%) and oxygen (47.6%); its C 1s bindings energies revealed the presence of C–C/C=C (284.7 eV), C–O (285.0 eV), C=O (288.1 eV), and O=C–OH (288.9 eV) units, and its O 1s binding energies suggested C=O (530.7 eV) and C–OH/C–O (531.5 eV) moieties (Fig. 4d–f). The XPS spectrum of CND-Bamboo II revealed that it contained carbon (66.0%) and oxygen (34.0%) atoms (Fig. 4g). Fig. 4h reveals C 1s binding energies for C–C/C=C (284.7 eV), C–O (285.2 eV), and C=O/O=C–OH (288.6 eV) groups; Fig. 4i reveals O 1s binding energies for C=O (530.9 eV) and C–OH/C–O (532.0 eV) units. The high percentages of carbon and oxygen atoms in these materials demonstrate that the carbonized bamboo and carbonized wood were highly oxidized. The functional groups revealed by this XPS data are consistent with those suggested by the FTIR spectra.

The XPS survey spectrum of CND-MO revealed the presence of carbon (66.9%), oxygen (28.0%), and nitrogen (5.1%) atoms; the C 1s binding energies revealed C–C/C=C (284.8 eV), C–N (285.8 eV), C–O (286.4 eV), and C=O/C=N (288.0 eV) functionalities; the N 1s binding energies revealed the presence of C=N (399.2 eV), C–N/NH_2 (399.7 eV), N–$(C)_3$ (400.3 eV), and N–H (401.5 eV) units, and the O 1s binding energies suggested C=O (531.5 eV) and C–O (532.5 eV) moieties (Fig. 5a–d). Thus, CND-MO possessed various amino units, especially secondary amino groups. The XPS survey spectrum of CND-PA revealed the presence of carbon (67.2%), oxygen (25.9%), and nitrogen (6.9%) atoms; that of CND-PB revealed carbon (63.7%), oxygen

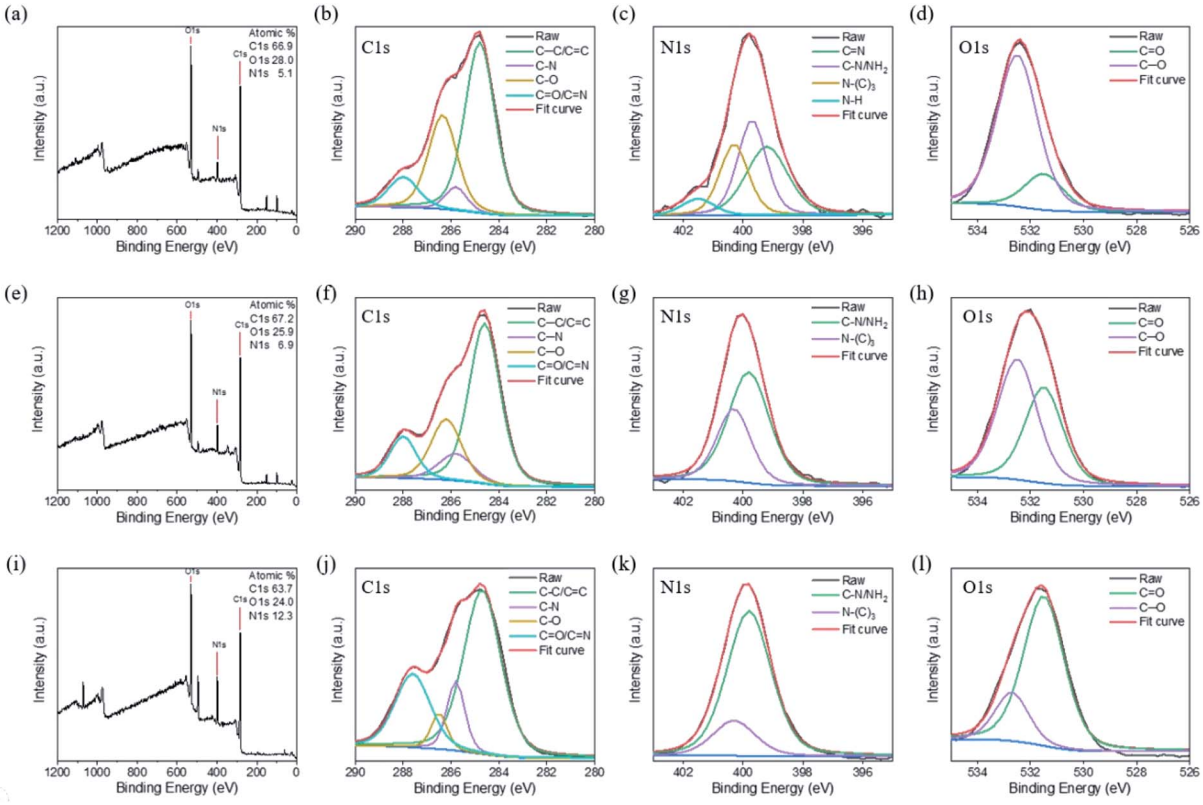

Fig. 5 XPS patterns of (a)–(d) CND-MO, (e)–(h) CND-PA, and (i)–(l) CND-PB: (a), (e) and (i) survey spectra; (b), (f) and (j) C 1s binding energies; (c), (g) and (k) N 1s binding energies; (d), (h) and (l) O 1s binding energies.

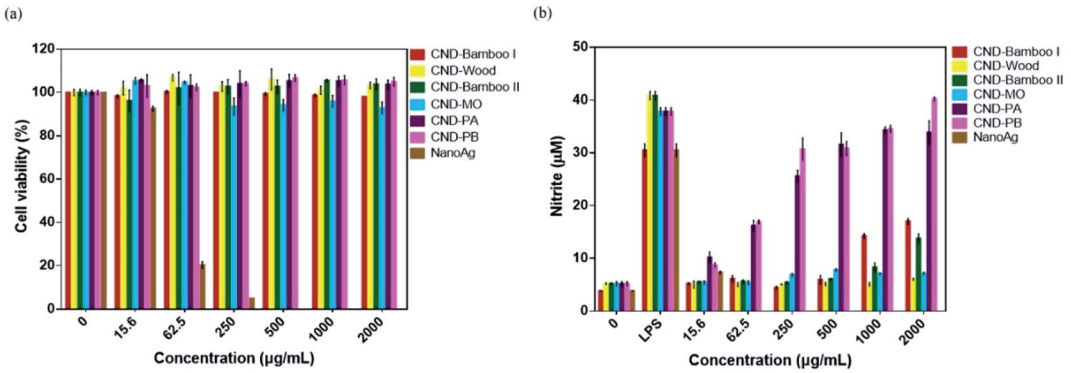

Fig. 6 (a) Cell viability of RAW264.7 cells treated with CNDs and NanoAg for 24 h, evaluated through MTT assays. (b) NO production of the cells treated with the CNDs and NanoAg, determined through NO assays.

(24.0%), and nitrogen (12.3%) atoms (Fig. 5e and i). We suspect that the precursor pineapples were grown in different regions, thereby producing different percentages of nitrogen atoms. As displayed in Fig. 5f and j, the C 1s binding energies in the XPS patterns of CND-PA and CND-PB revealed the presence of C–C/C=C (284.6 and 284.7 eV), C–N (285.8 eV), C–O (286.2 and 286.5 eV), and C=O/C=N (288.0 and 287.6 eV) functionalities; their N 1s binding energies suggested C–N/NH_2 (399.8 eV) and N–$(C)_3$ (400.3 eV) groups (Fig. 5g and k); in Fig. 5h and l, the O 1s binding energies imply C=O (531.5 eV) and C–O (532.5 and 532.7 eV) moieties. Thus, CND-PA and CND-PB possessed primary and tertiary amino units, with a higher intensity of the primary amino groups. Moreover, we also used XPS to analyze the compositions of the carbon, nitrogen, and oxygen atoms of the carbon precursors. The precursors of Bamboo I, Wood, and Bamboo II possessed nitrogen atom contents of less than 0.3%, whereas the precursors of MO, PA, and PB had values in the range from 2.7 to 4.7%. Based on the nitrogen atom contents of their precursors, our six types of CNDs containing high oxygen atom contents could be divided into two groups, with and

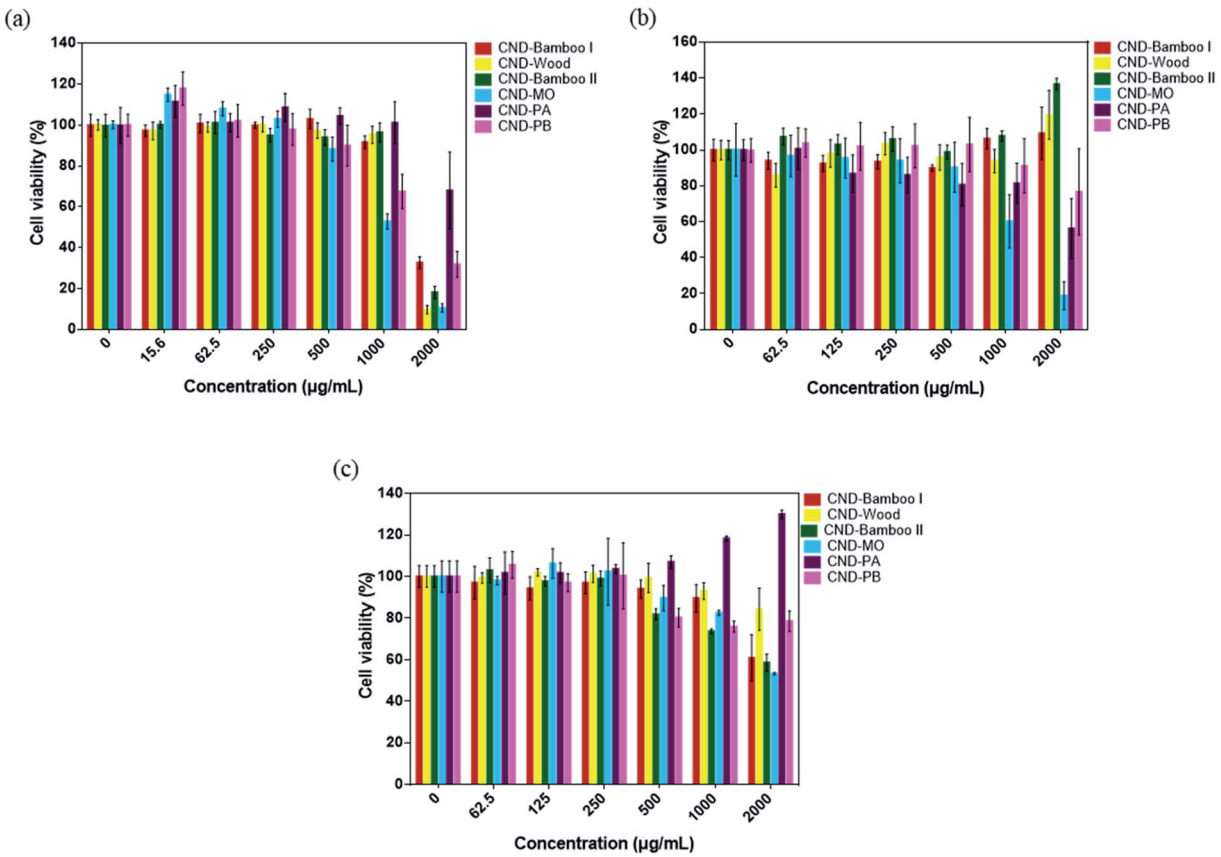

Fig. 7 Viabilities of (a) HacaT, (b) MCF-7, and (c) HT-29 cells after treatment with the series of CNDs for 48 h.

without nitrogen atom doping, depending on their various sources and treatment processes.

Table 1 summarizes the yields, QYs, optical properties, particle sizes, and atomic compositions of the CNDs. Briefly, the carbonized CNDs contained carbon and oxygen atoms, but the hydrothermally treated CNDs contained carbon, oxygen, and nitrogen atoms. The particle sizes of the carbonized and hydrothermally treated CNDs were approximately 3–5 nm, as determined using both dynamic light scattering and HRTEM. The QYs (calculated from the fluorescence properties and UV-Vis absorption spectra) were greater for CND-Bamboo I, CND-Wood, and CND-MO than they were for the other CNDs.

CND-Bamboo I, CND-Wood, CND-Bamboo II, CND-MO, CND-PA, and CND-PB displayed non-cytotoxicity toward treated RAW264.7 cells at 2000 μg mL; in contrast, NanoAg displayed cytotoxicity at a concentration of 62.5 μg mL^{-1}, with a cell viability of only 20% (Fig. 6a). LPS is a known endotoxin and a component of the cell wall of Gram-negative bacteria; it is widely used as a kind of activator for macrophages.[72] We performed an NO assay with LPS-treated RAW264.7 cells to ensure the formation of activated cells; we used them as our positive control. Our NO assays revealed whether the CNDs alone could produce inflammation, relative to the CNDs combined with LPS. CND-Bamboo I, CND-Wood, CND-Bamboo II, and CND-MO did not significantly increase the concentration of NO at a concentration of 500 μg mL^{-1}, but CND-PA and CND-PB increased the concentration of NO upon increasing the concentration of the CNDs. Concentrations of CND-Bamboo I and CND-Bamboo II of 1000 and 2000 μg mL^{-1}, respectively, did, however, increase the concentration of NO. CND-PA and CND-PB at 500 μg mL^{-1} induced the RAW264.7 cells to produce NO at concentrations above 30 μM. In contrast, NanoAg was cytotoxic toward the RAW264.7 cells at 62.5 μg mL; NO appeared when the concentration of NanoAg was as low as 15.6 μg mL^{-1}, but the concentration of NO did not increase significantly upon increasing its concentration thereafter (Fig. 6b). Increasing the concentration of CND-PA or CND-PB caused an increase in the amount of NO because these CNDs featured many primary amino groups in their structures and, therefore, may have induced inflammation.[73] NanoAg presumably exhibits cytotoxicity because it induces the generation of ROS that can damage cells. Moreover, Paul *et al.* revealed that AgNP-treated RAW264.7 cells displayed a cell viability of 33.99% at 70 μg mL^{-1}.[74]

We examined the series of CNDs through MTT assays with various cell lines; a cell viability of greater than 80% suggested that the CNDs possessed good biocompatibility and low cytotoxicity.[75,76] Treatment of HacaT cells with CND-Bamboo I, CND-Wood, CND-Bamboo II, and CND-PA revealed low cytotoxicity at 1000 μg mL; CND-MO and CND-PB displayed low cytotoxicity at 500 μg mL^{-1}. Notably, however, the CND-MO- and CND-PB-treated HacaT cells revealed cytotoxicity at 1000 and 2000 μg mL^{-1}, respectively, while CND-Bamboo I, CND-Wood, CND-Bamboo II, and CND-PA resulted in cytotoxicity at 2000 μg mL^{-1} (Fig. 7a). Fig. 7b and c reveal that CND-Bamboo I, CND-Wood, and CND-Bamboo II exhibited low cytotoxicity toward MCF-7 cells at 2000 μg mL; indeed, proliferation occurred at this concentration, presumably because the hydrophilic

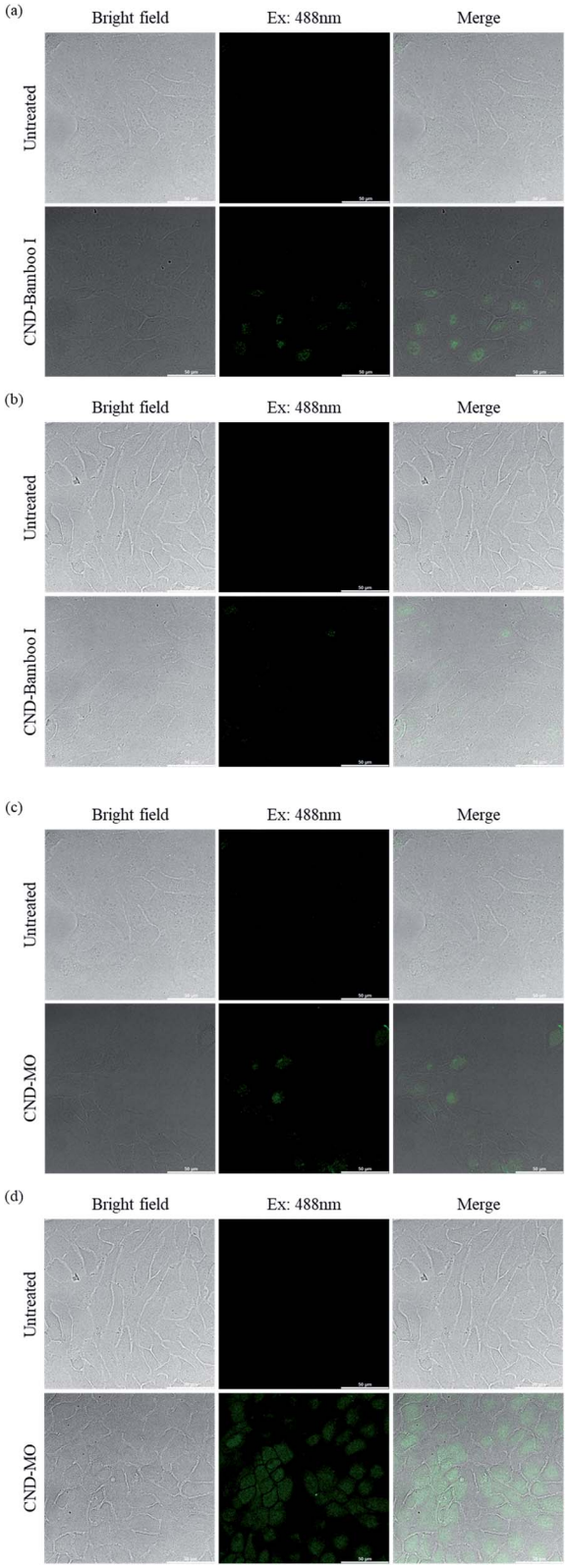

Fig. 8 Confocal microscopy images of HacaT cells, untreated and treated with (a) and (b) CND-Bamboo I and (c) and (d) CND-MO for (a) and (c) 6 and (b) and (d) 24 h.

functional groups and high oxygen atom content of the CNDs promoted cell adhesion in the hydrophilic environment.[77] The CND-MO-treated MCF-7 cells revealed cytotoxicity at 1000 μg mL; for CND-PA and CND-PB, cytotoxicity appeared at a concentration of 2000 μg mL^{-1}. The series of CNDs displayed low cytotoxicity toward HT-29 cells at a concentration of 500 μg mL^{-1}, but their cell viabilities varied upon treatment at 1000 and 2000 μg mL^{-1}. CND-Wood and CND-PB displayed low cytotoxicity at 2000 μg mL^{-1}, whereas CND-Bamboo I, CND-Bamboo II, and CND-MO were cytotoxic at this concentration. In contrast, CND-PA induced cell proliferation at 1000 and 2000 μg mL^{-1} (Fig. 7b). CND-MO featured secondary amino groups (*e.g.*, carbamate structures) that may have caused it to be stable toward the inhibition of MCF-7 and HT-29 cells.[78] CND-PA and CND-PB contained primary and tertiary amino groups; we suspect that CND-PA caused the proliferation of HT-29 because its many tertiary amino groups provided positive charge, recalling that hydrophilic functional groups promote cell proliferation.[79,80] Our CNDs of high oxygen atom content were less cytotoxic than our nitrogen-doped CNDs. Moreover, we treated the RAW 264.7 cells for 24 h and HacaT cells for 48 h to evaluate whether the six types of CNDs could induce toxicity within a short period of time when combined with drugs, and, therefore, whether these materials could be applied to wound dressing.[35] When the MCF-7 and HT-29 cells were treated for 48 h, our six types of CNDs displayed low toxicity at a concentration of 500 μg mL^{-1}, suggesting that they could be applied as nanocarriers.[31] In summary, the safe concentration of the six types of CNDs toward RAW264.7 cells was 2000 μg mL; toward HacaT, MCF-7, and HT-29 cells it was 500 μg mL^{-1}.

We used confocal microscopy to observe the behavior of our CNDs toward HacaT and MCF-7 cells. We selected these cells for bioimaging because CND-Bamboo I and CND-MO led to proliferation and inhibition, respectively, at high concentrations. Moreover, CND-Bamboo I and CND-MO exhibited more complete characteristics, including greater fluorescence, when compared with our other CNDs; note that CND-Bamboo I and CND-MO are high-oxygen-content CNDs without and with nitrogen-doping, respectively. For the HacaT cells, CND-Bamboo I underwent excitation at 488 nm and displayed emission between 500 and 550 nm; CND-MO underwent excitation at 488 nm, with emission at 500–550 nm. For the MCF-7 cells, CND-Bamboo I underwent excitation at 488 nm, with emission between 500 and 550 nm; CND-MO underwent excitation at 488 nm, with emission at 500–550 nm. The confocal images revealed that the fluorescence was located inside the cells when the HacaT cells were treated with CND-Bamboo I for 6 h; after 24 h, the treated HacaT cells displayed less fluorescence, presumably because of chemical degradation or exocytosis (Fig. 8a and b).[81] CND-MO displayed less fluorescence when the HacaT cells had been treated for 6 h; after 24 h, however, the CND-MO-treated HacaT cells displayed greater fluorescence from within (Fig. 8c and d). Thus, our high-oxygen-content CNDs without and with nitrogen-doping exhibited different behavior when treating normal cells for different periods of time. The confocal images revealed that the control groups of MCF-7 cells exhibited autofluorescence.[66] CND-

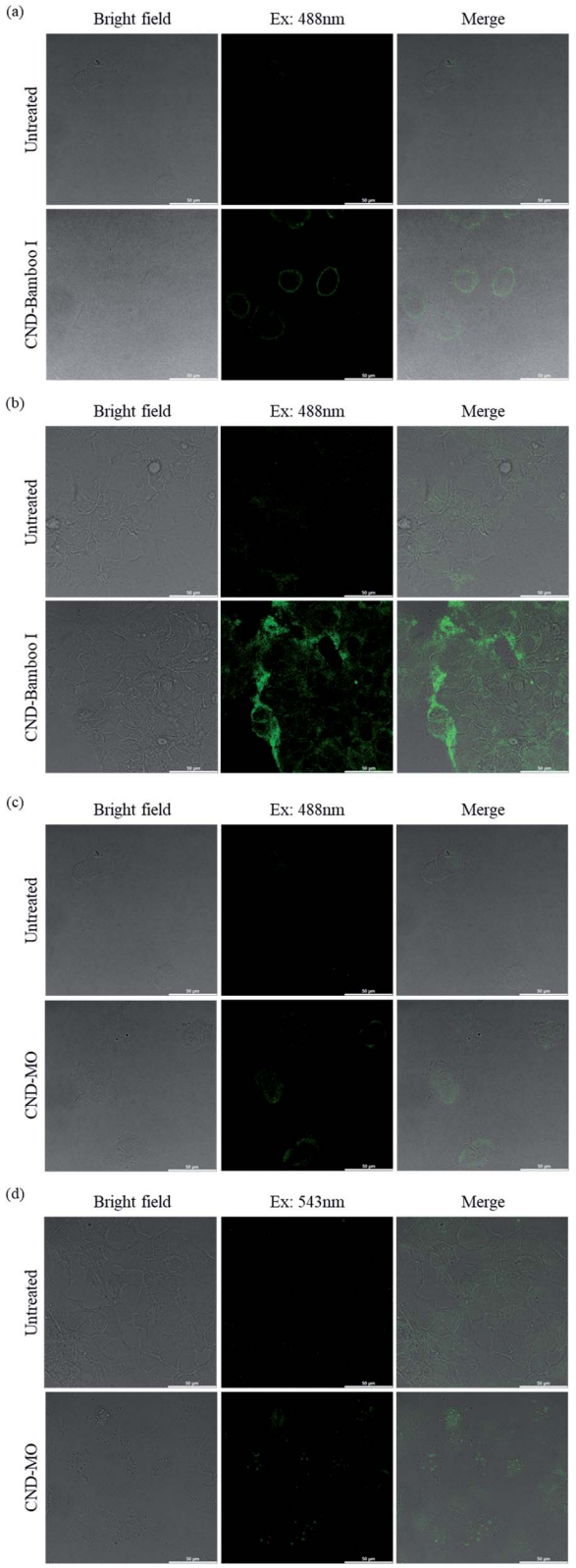

Fig. 9 Confocal microscopy images of MCF-7 cells, untreated and treated with (a) and (b) CND-Bamboo I and (c) and (d) CND-MO for (a) and (c) 6 and (b) and (d) 24 h.

Bamboo I was located on the cell membrane after treating the MCF-7 cells for 6 h, but it was located within the cells after 24 h (Fig. 9a and b). The confocal images revealed that CND-Bamboo I, with its high oxygen content and hydrophilic functional groups, attached to the cell membrane; thus, it was possible to promote the cell adhesion in a hydrophilic environment. The CND-MO-treated MCF-7 cells displayed fluorescence inside the cells after 6 and 24 h (Fig. 9c and d). Notably, for imaging of the MCF-7 cells after 24 h, CND-MO was excited at 543 nm, with emission between 555 and 620 nm, because excitation at 488 nm resulted in non-fluorescence (Fig. 9d).

4. Conclusion

We have prepared CNDs from natural plants and agricultural waste through eco-friendly and rapid carbonization and hydrothermal processes. Our carbon sources were bamboo, wood, a natural herb, and pineapple. Our six types of CNDs displayed fluorescence and possessed nanoscale dimensions; they could be divided into two groups – of high oxygen content with and without nitrogen-doping – that displayed different biological activities at high concentration. The safe concentration of the six types of CNDs toward RAW264.7 cells, at which they displayed non-cytotoxicity, was 2000 μg mL; they displayed low cytotoxicity toward HacaT, MCF-7, and HT-29 cells at 500 μg mL^{-1}. Confocal microscopy images revealed the fluorescence of CND-Bamboo I and CND-MO when mixed with HacaT and MCF-7 cells.

Conflicts of interest

The authors declare no competing financial interest.

Acknowledgements

This study was supported by research grants from the National Science Council of Taiwan (grant nos. MOST 106-2113-M-039-007 and MOST 108-2113-M-039-003) and China Medical University (grant nos. CMU108-AWARD-01 and CMU-108-MF-122).

References

1 P. Namdari, B. Negahdari and A. Eatemadi, Synthesis, properties and biomedical applications of carbon-based quantum dots: An updated review, *Biomed. Pharmacother.*, 2017, **87**, 209–222.
2 X. Y. Xu, R. Ray, Y. L. Gu, H. J. Ploehn, L. Gearheart, K. Raker and W. A. Scrivens, Electrophoretic analysis and purification of fluorescent single-walled carbon nanotube fragments, *J. Am. Chem. Soc.*, 2004, **126**(40), 12736–12737.
3 J. Chen, Y. Li, K. Lv, W. B. Zhong, H. Wang, Z. Wu, P. G. Yi and J. H. Jiang, Cyclam-functionalized carbon dots sensor for sensitive and selective detection of copper(II) ion and sulfide anion in aqueous media and its imaging in live cells, *Sens. Actuators, B*, 2016, **224**, 298–306.
4 A. Sharma and J. Das, Small molecules derived carbon dots: synthesis and applications in sensing, catalysis, imaging, and biomedicine, *J. Nanobiotechnol.*, 2019, **17**(1), 92.
5 D. Carolan, C. Rocks, D. B. Padmanaban, P. Maguire, V. Svrcek and D. Mariotti, Environmentally friendly nitrogen-doped carbon quantum dots for next generation solar cells, *Sustainable Energy Fuels*, 2017, **1**(7), 1611–1619.
6 T. Y. Juang, J. C. Kao, J. C. Wang, S. Y. Hsu and C. P. Chen, Carbonized Bamboo-Derived Carbon Nanodots as Efficient Cathode Interfacial Layers in High-Performance Organic Photovoltaics, *Adv. Mater. Interfaces*, 2018, **5**(10), 1800031.
7 H.-L. Hsu, H.-T. Hsiao, T.-Y. Juang, B.-H. Jiang, S.-C. Chen, R.-J. Jeng and C.-P. Chen, Carbon Nanodot Additives Realize High-Performance Air-Stable p–i–n Perovskite Solar Cells Providing Efficiencies of up to 20.2%, *Adv. Energy Mater.*, 2018, **8**, 1802323.
8 W. Li, Q. Liu, P. Zhang and L. Liu, Zwitterionic nanogels crosslinked by fluorescent carbon dots for targeted drug delivery and simultaneous bioimaging, *Acta Biomater.*, 2016, **40**, 254–262.
9 A. Dehghani, S. M. Ardekani, M. Hassan and V. G. Gomes, Collagen derived carbon quantum dots for cell imaging in 3D scaffolds via two-photon spectroscopy, *Carbon*, 2018, **131**, 238–245.
10 N. K. R. Bogireddy, J. Lara, L. R. Fragoso and V. Agarwal, One-step hydrothermal preparation of highly stable N doped oxidized carbon dots for toxic organic pollutants sensing and bioimaging, *Chem. Eng. J.*, 2020, **401**, 126097.
11 S. Kainth, B. Maity and S. Basu, Label-free detection of creatinine using nitrogen-passivated fluorescent carbon dots, *RSC Adv.*, 2020, **10**(60), 36253–36264.
12 S. A. Nicolae, H. Au, P. Modugno, H. Luo, A. E. Szego, M. Qiao, L. Li, W. Yin, H. J. Heeres, N. Berge and M.-M. Titirici, Recent advances in hydrothermal carbonisation: from tailored carbon materials and biochemicals to applications and bioenergy, *Green Chem.*, 2020, **22**(15), 4747–4800.
13 M. Si, J. Zhang, Y. He, Z. Yang, X. Yan, M. Liu, S. Zhuo, S. Wang, X. Min, C. Gao, L. Chai and Y. Shi, Synchronous and rapid preparation of lignin nanoparticles and carbon quantum dots from natural lignocellulose, *Green Chem.*, 2018, **20**(15), 3414–3419.
14 R. Mohammadinejad, S. Karimi, S. Iravani and R. S. Varma, Plant-derived nanostructures: types and applications, *Green Chem.*, 2016, **18**(1), 20–52.
15 K. W. Chu, S. L. Lee, C. J. Chang and L. Y. Liu, Recent Progress of Carbon Dot Precursors and Photocatalysis Applications, *Polymers*, 2019, **11**(4), 689.
16 Y. H. Liu, H. Huang, W. J. Cao, B. D. Mao, Y. Liu and Z. H. Kang, Advances in carbon dots: from the perspective of traditional quantum dots, *Mater. Chem. Front.*, 2020, **4**(6), 1586–1613.
17 Y. Chong, Y. F. Ma, H. Shen, X. L. Tu, X. Zhou, J. Y. Xu, J. W. Dai, S. J. Fan and Z. J. Zhang, The in vitro and in vivo toxicity of graphene quantum dots, *Biomaterials*, 2014, **35**(19), 5041–5048.

18 Z. L. Peng, X. Han, S. H. Li, A. O. Al-Youbi, A. S. Bashammakh, M. S. El-Shahawi and R. M. Leblanc, Carbon dots: biomacromolecule interaction, bioimaging and nanomedicine, *Coord. Chem. Rev.*, 2017, **343**, 256–277.

19 M. Semeniuk, Z. H. Yi, V. Poursorkhabi, J. Tjong, S. Jaffer, Z. H. Lu and M. Sain, Future Perspectives and Review on Organic Carbon Dots in Electronic Applications, *ACS Nano*, 2019, **13**(6), 6224–6255.

20 M. L. Liu, B. B. Chen, C. M. Li and C. Z. Huang, Carbon dots: synthesis, formation mechanism, fluorescence origin and sensing applications, *Green Chem.*, 2019, **21**(3), 449–471.

21 V. Sharma, P. Tiwari and S. M. Mobin, Sustainable carbon-dots: recent advances in green carbon dots for sensing and bioimaging, *J. Mater. Chem. B*, 2017, **5**(45), 8904–8924.

22 S. S. P. Nair, N. Kottam and S. G. Prasanna Kumar, Green synthesized luminescent carbon nanodots for the sensing application of Fe^{3+} ions, *J. Fluoresc.*, 2020, **30**(2), 357–363.

23 A. Anand, B. Unnikrishnan, S. C. Wei, C. P. Chou, L. Z. Zhang and C. C. Huang, Graphene oxide and carbon dots as broad-spectrum antimicrobial agents - a minireview, *Nanoscale Horiz.*, 2019, **4**(1), 117–137.

24 N. Kottam and S. Smrithi, Luminescent carbon nanodots: current prospects on synthesis, properties and sensing applications, *Methods Appl. Fluoresc.*, 2021, **9**(1), 012001.

25 R. Jijie, A. Barras, J. Bouckaert, N. Dumitrascu, S. Szunerits and R. Boukherroub, Enhanced antibacterial activity of carbon dots functionalized with ampicillin combined with visible light triggered photodynamic effects, *Colloids Surf., B*, 2018, **170**, 347–354.

26 T. Feng and Y. Zhao, Preparation of Responsive Carbon Dots for Anticancer Drug Delivery, *Methods Mol. Biol.*, 2019, **2000**, 227–234.

27 M. Omidi, A. Yadegari and L. Tayebi, Wound dressing application of pH-sensitive carbon dots/chitosan hydrogel, *RSC Adv.*, 2017, **7**(18), 10638–10649.

28 P. J. G. Luo, S. Sahu, S. T. Yang, S. K. Sonkar, J. P. Wang, H. F. Wang, G. E. LeCroy, L. Cao and Y. P. Sun, Carbon "quantum" dots for optical bioimaging, *J. Mater. Chem. B*, 2013, **1**(16), 2116–2127.

29 S. D. Hettiarachchi, R. M. Graham, K. J. Mintz, Y. Q. Zhou, S. Vanni, Z. L. Peng and R. M. Leblanc, Triple conjugated carbon dots as a nano-drug delivery model for glioblastoma brain tumors, *Nanoscale*, 2019, **11**(13), 6192–6205.

30 W. J. Liu, C. Li, Y. J. Ren, X. B. Sun, W. Pan, Y. H. Li, J. P. Wang and W. J. Wang, Carbon dots: surface engineering and applications, *J. Mater. Chem. B*, 2016, **4**(35), 5772–5788.

31 M. Zhang, P. Yuan, N. L. Zhou, Y. T. Su, M. N. Shao and C. Chi, pH-Sensitive N-doped carbon dots-heparin and doxorubicin drug delivery system: preparation and anticancer research, *RSC Adv.*, 2017, **7**(15), 9347–9356.

32 T. T. Sun, M. Zheng, Z. G. Xie and X. B. Jinga, Supramolecular hybrids of carbon dots with doxorubicin: synthesis, stability and cellular trafficking, *Mater. Chem. Front.*, 2017, **1**(2), 354–360.

33 Z. Y. Wang, H. Liao, H. Wu, B. B. Wang, H. D. Zhao and M. Q. Tan, Fluorescent carbon dots from beer for breast cancer cell imaging and drug delivery, *Anal. Methods*, 2015, **7**(20), 8911–8917.

34 K. Bankoti, A. P. Rameshbabu, S. Datta, B. Das, A. Mitra and S. Dhara, Onion derived carbon nanodots for live cell imaging and accelerated skin wound healing, *J. Mater. Chem. B*, 2017, **5**(32), 6579–6592.

35 Y. J. Li, S. G. Harroun, Y. C. Su, C. F. Huang, B. Unnikrishnan, H. J. Lin, C. H. Lin and C. C. Huang, Synthesis of Self-Assembled Spermidine-Carbon Quantum Dots Effective against Multidrug-Resistant Bacteria, *Adv. Healthcare Mater.*, 2016, **5**(19), 2545–2554.

36 H. J. Jian, R. S. Wu, T. Y. Lin, Y. J. Li, H. J. Lin, S. G. Harroun, J. Y. Lai and C. C. Huang, Super-Cationic Carbon Quantum Dots Synthesized from Spermidine as an Eye Drop Formulation for Topical Treatment of Bacterial Keratitis, *ACS Nano*, 2017, **11**(7), 6703–6716.

37 Y. H. Lee, F. Y. Cheng, H. W. Chiu, J. C. Tsai, C. Y. Fang, C. W. Chen and Y. J. Wang, Cytotoxicity, oxidative stress, apoptosis and the autophagic effects of silver nanoparticles in mouse embryonic fibroblasts, *Biomaterials*, 2014, **35**(16), 4706–4715.

38 Y. H. Lee, C. Y. Fang, H. W. Chiu, F. Y. Cheng, J. C. Tsai, C. W. Chen and Y. J. Wang, Endoplasmic Reticulum Stress-Triggered Autophagy and Lysosomal Dysfunction Contribute to the Cytotoxicity of Amine-Modified Silver Nanoparticles in NIH 3T3 Cells, *J. Biomed. Nanotechnol.*, 2017, **13**(7), 778–794.

39 Y. C. Liu, Y. Y. Hsiao, K. L. Ku, H. F. Liao and W. C. Chao, Mahonia oiwakensis Extract and Its Bioactive Compounds Exert Anti-inflammatory Activities and VEGF Production Through M2-Macrophagic Polarization and STAT6 Activation, *J. Med. Food*, 2018, **21**(7), 654–664.

40 J. Chao, T. C. Lu, J. W. Liao, T. H. Huang, M. S. Lee, H. Y. Cheng, L. K. Ho, C. L. Kuo and W. H. Peng, Analgesic and anti-inflammatory activities of ethanol root extract of Mahonia oiwakensis in mice, *J. Ethnopharmacol.*, 2009, **125**(2), 297–303.

41 W. Yang, C.-Y. Pan, X.-Q. Liu and J. Wang, Multiple functional hyperbranched poly (amido amine) nanoparticles: synthesis and application in cell imaging, *Biomacromolecules*, 2011, **12**(5), 1523–1531.

42 I. Grabchev, P. Bosch, M. McKenna and D. Staneva, A new colorimetric and fluorimetric sensor for metal cations based on poly(propylene amine) dendrimer modified with 1,8-naphthalimide, *J. Photochem. Photobiol., A*, 2009, **201**(1), 75–80.

43 H. Ding, X. H. Li, X. B. Chen, J. S. Wei, X. B. Li and H. M. Xiong, Surface states of carbon dots and their influences on luminescence, *J. Appl. Phys.*, 2020, **127**(23), 231101.

44 L. Wang, M. Li, W. T. Li, Y. Han, Y. J. Liu, Z. Li, B. H. Zhang and D. Y. Pan, Rationally Designed Efficient Dual-Mode Colorimetric/Fluorescence Sensor Based on Carbon Dots for Detection of pH and Cu^{2+} Ions, *ACS Sustainable Chem. Eng.*, 2018, **6**(10), 12668–12674.

45 J. Joseph and A. A. Anappara, White light emission of carbon dots by creating different emissive traps, *J. Lumin.*, 2016, **178**, 128–133.
46 H. Ding, L. W. Cheng, Y. Y. Ma, J. L. Kong and H. M. Xiong, Luminescent carbon quantum dots and their application in cell imaging, *New J. Chem.*, 2013, **37**(8), 2515–2520.
47 A. Dager, T. Uchida, T. Maekawa and M. Tachibana, Synthesis and Characterization of Mono-disperse Carbon Quantum Dots from Fennel Seeds: Photoluminescence Analysis Using Machine Learning, *Sci. Rep.*, 2019, **9**, 1–12.
48 J. Liao, Z. H. Cheng and L. Zhou, Nitrogen-Doping Enhanced Fluorescent Carbon Dots: Green Synthesis and Their Applications for Bioimaging and Label-Free Detection of Au^{3+} Ions, *ACS Sustainable Chem. Eng.*, 2016, **4**(6), 3053–3061.
49 W. N. Yang, H. Zhang, J. X. Lai, X. Y. Peng, Y. P. Hu, W. Gu and L. Ye, Carbon dots with red-shifted photoluminescence by fluorine doping for optical bio-imaging, *Carbon*, 2018, **128**, 78–85.
50 H. Ding, J. S. Wei and H. M. Xiong, Nitrogen and sulfur co-doped carbon dots with strong blue luminescence, *Nanoscale*, 2014, **6**(22), 13817–13823.
51 Q. Xu, Y. Liu, R. G. Su, L. L. Cai, B. F. Li, Y. Y. Zhang, L. Z. Zhang, Y. J. Wang, Y. Wang, N. Li, X. Gong, Z. P. Gu, Y. S. Chen, Y. L. Tan, C. B. Dong and T. S. Sreeprasad, Highly fluorescent Zn-doped carbon dots as Fenton reaction-based bio-sensors: an integrative experimental-theoretical consideration, *Nanoscale*, 2016, **8**(41), 17919–17927.
52 H. Li, Z. Kang, Y. Liu and S.-T. Lee, Carbon nanodots: synthesis, properties and applications, *J. Mater. Chem.*, 2012, **22**(46), 24230–24253.
53 X. M. Wei, Y. Xu, Y. H. Li, X. B. Yin and X. W. He, Ultrafast synthesis of nitrogen-doped carbon dots via neutralization heat for bioimaging and sensing applications, *RSC Adv.*, 2014, **4**(84), 44504–44508.
54 V. Arul and M. G. Sethuraman, Hydrothermally Green Synthesized Nitrogen-Doped Carbon Dots from Phyllanthus emblica and Their Catalytic Ability in the Detoxification of Textile Effluents, *ACS Omega*, 2019, **4**(2), 3449–3457.
55 G. S. Tong, J. X. Wang, R. B. Wang, X. Q. Guo, L. He, F. Qiu, G. Wang, B. S. Zhu, X. Y. Zhu and T. Liu, Amorphous carbon dots with high two-photon fluorescence for cellular imaging passivated by hyperbranched poly(amino amine), *J. Mater. Chem. B*, 2015, **3**(4), 700–706.
56 J. Zhou, X. Y. Shan, J. J. Ma, Y. M. Gu, Z. S. Qian, J. R. Chen and H. Feng, Facile synthesis of P-doped carbon quantum dots with highly efficient photoluminescence, *RSC Adv.*, 2014, **4**(11), 5465–5468.
57 K. Linehan and H. Doyle, Solution reduction synthesis of amine terminated carbon quantum dots, *RSC Adv.*, 2014, **4**(24), 12094–12097.
58 Q. Wang, C. L. Zhang, G. X. Shen, H. Y. Liu, H. L. Fu and D. X. Cui, Fluorescent carbon dots as an efficient siRNA nanocarrier for its interference therapy in gastric cancer cells, *J. Nanobiotechnol.*, 2014, **12**, 1–12.
59 F. S. Wu, H. F. Su, K. Wang, W. K. Wong and X. J. Zhu, Facile synthesis of N-rich carbon quantum dots from porphyrins as efficient probes for bioimaging and biosensing in living cells, *Int. J. Nanomed.*, 2017, **12**, 7375–7391.
60 A. Tadesse, M. Hagos, D. RamaDevi, K. Basavaiah and N. Belachew, Fluorescent-Nitrogen-Doped Carbon Quantum Dots Derived from Citrus Lemon Juice: Green Synthesis, Mercury(II) Ion Sensing, and Live Cell Imaging, *ACS Omega*, 2020, **5**(8), 3889–3898.
61 C. Lee, K. Dazen, K. Kafle, A. Moore, D. K. Johnson, S. Park and S. H. Kim, Correlations of Apparent Cellulose Crystallinity Determined by XRD, NMR, IR, Raman, and SFG Methods, *Adv. Polym. Sci.*, 2016, **271**, 115–131.
62 J. Gong, J. Li, J. Xu, Z. Y. Xian and L. H. Mo, Research on cellulose nanocrystals produced from cellulose sources with various polymorphs, *RSC Adv.*, 2017, **7**(53), 33486–33493.
63 Z. Ouyang, Y. Lei, Y. P. Chen, Z. Zhang, Z. C. Jiang, J. X. Hu and Y. Y. Lin, Preparation and Specific Capacitance Properties of Sulfur, Nitrogen Co-Doped Graphene Quantum Dots, *Nanoscale Res. Lett.*, 2019, **14**, 1–9.
64 M. L. Liu, L. Yang, R. S. Li, B. B. Chen, H. Liu and C. Z. Huang, Large-scale simultaneous synthesis of highly photoluminescent green amorphous carbon nanodots and yellow crystalline graphene quantum dots at room temperature, *Green Chem.*, 2017, **19**(15), 3611–3617.
65 K. Habiba, V. I. Makarov, J. Avalos, M. J. F. Guinel, B. R. Weiner and G. Morell, Luminescent graphene quantum dots fabricated by pulsed laser synthesis, *Carbon*, 2013, **64**, 341–350.
66 N. Vasimalai, V. Vilas-Boas, J. Gallo, M. D. Cerqueira, M. Menendez-Miranda, J. M. Costa-Fernandez, L. Dieguez, B. Espina and M. T. Fernandez-Arguelles, Green synthesis of fluorescent carbon dots from spices for in vitro imaging and tumour cell growth inhibition, *Beilstein J. Nanotechnol.*, 2018, **9**, 530–544.
67 H. Q. Zhang, P. W. Dai, L. Z. Huang, Y. H. Huang, Q. T. Huang, W. X. Zhang, C. Wei and S. R. Hu, A nitrogen-doped carbon dot/ferrocene@beta-cyclodextrin composite as an enhanced material for sensitive and selective determination of uric acid, *Anal. Methods*, 2014, **6**(8), 2687–2691.
68 A. Kurdekar, L. A. A. Chunduri, E. P. Bulagonda, M. K. Haleyurgirisetty, V. Kamisetti and I. K. Hewlett, Comparative performance evaluation of carbon dot-based paper immunoassay on Whatman filter paper and nitrocellulose paper in the detection of HIV infection, *Microfluid. Nanofluid.*, 2016, **20**(7), 1–13.
69 S. S. Lu, S. S. Guo, P. X. Xu, X. R. Li, Y. M. Zhao, W. Gu and M. Xue, Hydrothermal synthesis of nitrogen-doped carbon dots with real-time live-cell imaging and blood-brain barrier penetration capabilities, *Int. J. Nanomed.*, 2016, **11**, 6325–6336.
70 R. Shi, Z. Li, H. J. Yu, L. Shang, C. Zhou, G. I. N. Waterhouse, L. Z. Wu and T. R. Zhang, Effect of Nitrogen Doping Level on the Performance of N-Doped Carbon Quantum Dot/TiO_2

Composites for Photocatalytic Hydrogen Evolution, *Chemsuschem*, 2017, **10**(22), 4650–4656.

71 Z. Han, D. Y. Nan, H. Yang, Q. Q. Sun, S. Pan, H. Liu and X. L. Hu, Carbon quantum dots based ratiometric fluorescence probe for sensitive and selective detection of Cu^{2+} and glutathione, *Sens. Actuators, B*, 2019, **298**.

72 T. Joo, K. Sowndhararajan, S. Hong, J. Lee, S. Y. Park, S. Kim and J. W. Jhoo, Inhibition of nitric oxide production in LPS-stimulated RAW 264.7 cells by stem bark of Ulmus pumila L, *Saudi J. Biol. Sci.*, 2014, **21**(5), 427–435.

73 R. Toy, P. Pradhan, V. Ramesh, N. C. Di Paolo, B. Lash, J. Y. Liu, E. L. Blanchard, C. J. Pinelli, P. J. Santangelo, D. M. Shayakhmetov and K. Roy, Modification of primary amines to higher order amines reduces in vivo hematological and immunotoxicity of cationic nanocarriers through TLR4 and complement pathways, *Biomaterials*, 2019, **225**, 119512.

74 A. Paul, H. Ju, S. Rangasamy, Y. Shim and J. M. Song, Nanosized silver(II) pyridoxine complex to cause greater inflammatory response and less cytotoxicity to RAW264.7 macrophage cells, *Nanoscale Res. Lett.*, 2015, **10**, 140.

75 X. C. Yuan, Z. M. Liu, Z. Y. Guo, Y. H. Ji, M. Jin and X. P. Wang, Cellular distribution and cytotoxicity of graphene quantum dots with different functional groups, *Nanoscale Res. Lett.*, 2014, **9**, 1–9.

76 P. Ramachandran, C. Y. Lee, R. A. Doong, C. E. Oon, N. T. K. Thanh and H. L. Lee, A titanium dioxide/nitrogen-doped graphene quantum dot nanocomposite to mitigate cytotoxicity: synthesis, characterisation, and cell viability evaluation, *RSC Adv.*, 2020, **10**(37), 21795–21805.

77 H. G. Oh, H. G. Nam, D. H. Kim, M. H. Kim, K. H. Jhee and K. S. Song, Neuroblastoma cells grown on fluorine or oxygen treated graphene sheets, *Mater. Lett.*, 2014, **131**, 328–331.

78 A. K. Ghosh and M. Brindisi, Organic Carbamates in Drug Design and Medicinal Chemistry, *J. Med. Chem.*, 2015, **58**(7), 2895–2940.

79 W. Zhang, N. Liu, H. G. Shi, J. Liu, L. X. Shi, B. Zhang, H. Y. Wang, J. H. Ji and P. K. Chu, Upregulation of BMSCs Osteogenesis by Positively-Charged Tertiary Amines on Polymeric Implants via Charge/iNOS Signaling Pathway, *Sci. Rep.*, 2015, **5**, 1–10.

80 A. Jarosz, M. Skoda, I. Dudek and D. Szukiewicz, Oxidative Stress and Mitochondrial Activation as the Main Mechanisms Underlying Graphene Toxicity against Human Cancer Cells, *Oxid. Med. Cell. Longevity*, 2016, **2016**, 5851035.

81 N. Zhou, S. J. Zhu, S. Maharjan, Z. Y. Hao, Y. B. Song, X. H. Zhao, Y. F. Jiang, B. Yang and L. J. Lu, Elucidating the endocytosis, intracellular trafficking, and exocytosis of carbon dots in neural cells, *RSC Adv.*, 2014, **4**(107), 62086–62095.